PAPER • OPEN ACCESS

2D measurements of parallel counter-streaming flows in the W7-X scrape-off layer for attached and detached plasmas

View the article online for updates and enhancements.

2D measurements of parallel counter-streaming flows in the W7-X scrape-off layer for attached and detached plasmas

V. Perseo[1,*], **V. Winters**[1], **Y. Feng**[1], **F. Reimold**[1], **O.P. Ford**[1], **R. König**[1],
S.A. Bozhenkov[1], **K.J. Brunner**[1], **R. Burhenn**[1], **P. Drewelow**[1],
D.A. Ennis[2], **Y. Gao**[1], **D. Gradic**[1], **P. Hacker**[1], **U. Hergenhahn**[1,4],
M.W. Jakubowski[1], **J. Knauer**[1], **T. Kremeyer**[1], **D.M. Kriete**[2],
M. Krychowiak[1], **S. Kwak**[1], **H. Niemann**[1], **A. Pavone**[1], **F. Pisano**[3],
A. Puig Sitjes[1], **G. Schlisio**[1], **J. Svensson**[1], **D. Zhang**[1],
T. Sunn Pedersen[1] **and the W7-X Team**[1,a]

[1] Max-Planck-Institut für Plasmaphysik, 17491 Greifswald, Germany
[2] Auburn University, 36849 Auburn, AL, United States of America
[3] University of Cagliari, 09124 Cagliari, Italy

E-mail: valeria.perseo@ipp.mpg.de

CrossMark

Abstract

Investigations of particle parallel flow velocities have been carried out for the scrape-off layer (SOL) of the Wendelstein 7-X (W7-X) stellarator, in order to gain insights on the SOL transport properties during attached and detached plasma scenarios. The experimental evidence is based on the coherence imaging spectroscopy (CIS) diagnostic, able to measure 2D impurity emission intensity and flow velocity. The impurity monitored by CIS is C^{2+}, characterized by a line-emission intensity observed to be linearly proportional to the total plasma radiated power in both attached and detached plasmas. The related C^{2+} velocity shows a strong dependence on the line-averaged electron density while remaining insensitive to the input power. During attached plasmas, the velocity increases with increasing line-averaged density. The tendency reverses in the transition to and during detachment, in which the velocity decreases by at least a factor of 2. The sharp drop in velocity, together with a rise in line-emission intensity, is reliably correlated to the detachment transition and can therefore be used as one of its signatures. The impurity flow velocity appears to be well coupled with the main ions' one, thus implying the dominant role of impurity-main ion friction in the parallel impurity transport dynamics. In view of this SOL impurity transport regime, the CIS

---

measurement results are here interpreted with the help of EMC3-Eirene simulations, and their major trends are already explainable with a simple 1D fluid model.

(Some figures may appear in colour only in the online journal)

1. Introduction

Understanding the scrape-off layer (SOL) physics in current fusion devices is essential to solve the exhaust problem for future reactors. The SOL configuration determines the intersections between the magnetic field lines and the divertor targets, opening up parallel transport channels for plasma heat and particles, which represent the most direct way for the exhaust to reach the dedicated areas with heat sinks and pumps [1]. The interplay of parallel and perpendicular transport, along with the distribution of sources, sets the SOL dynamics for both particles and energy, and consequently defines the effectiveness of a particular divertor configuration. Investigating the parallel particle flows can therefore give insights into the overall SOL behaviour [2], allowing the assessment of the predominant flow directions of the main plasma ions and impurities, and to have a direct representation of convective heat transport. Despite the fact that ion convection is commonly considered negligible in the description of the total divertor heat deposition [1], recent results at DIII-D for attached plasmas point out how the standard model based on electron conduction dominance is not always valid [3]. For the Wendelstein 7-X (W7-X) stellarator, characterized by the *island divertor configuration* [4], a more significant role of convection is to be expected, as the characteristic SOL temperature gradients are weaker and the connection lengths longer than typically in tokamaks [5, 6]. An analysis of the parallel particle flows is hence confirmed to be a prerequisite to the understanding of the general SOL transport properties, even for heat deposition. Moreover, particle flows appear to be difficult to capture in modelling [7, 8], pointing to the necessity of direct measurements to identify deficiencies in the models and to improve the simulation results.

In order to perform successful studies of the SOL parallel transport, it is necessary to rely on dedicated edge diagnostics. A powerful tool that has recently emerged is the coherence imaging spectroscopy (CIS) diagnostic, a camera-based interferometric system capable of measuring Doppler particle flows associated with a selected visible emission line from the plasma [9, 10]. The wavelength shift associated with the Doppler velocities is encoded in a 2D interference pattern, which is reliably and precisely decoded thanks to the application of fast Fourier transforms and dedicated calibration measurements [10–12]. In contrast to other flow diagnostics such as dispersive spectroscopy and Mach probes, CIS is distinguished by providing high time and flow velocity resolution, and high spatial coverage simultaneously. Its 2D spatially

resolved measurements led to the first direct detection of the complex 3D counter-streaming parallel flows structure in the SOL of W7-X [13]. The observation stands out as one of the earliest pieces of experimental evidence for the existence of a parallel friction-dominated impurity transport regime in the W7-X islands, which was heretofore only a theoretical prediction [6]. The W7-X CIS application involves passive measurements of C^{2+} impurities (via the C III 465 nm transition line) during hydrogen plasma experiments, with a view over the entire SOL and lines of sight nearly tangential to the magnetic field. The choice of carbon as impurity under investigation is justified by the fact that this species is expected to be one of the main radiators in W7-X due to its graphite plasma facing components [14]. The C^{2+} line-of-sight integrated measurements are restricted to the edge of the machine by the temperature dependence of the charged state emission, which peak in the range of 10–20 eV [1]. An example of the CIS results for C^{2+} flow velocity and radiation intensity can be found in figure 1. The displayed experiment was performed in the *standard* magnetic configuration, characterized by an island chain in the SOL formed by 5 independent islands [15]. The chosen time point is characterized by input power $P_{ECRH} = 2.5$ MW and line-averaged density $\overline{n}_e = 5.65 \times 10^{19}$ m^{-2}. The patterns of both C^{2+} flow velocity and radiation intensity are influenced by the structure of the island chain. The flow velocities are defined as positive (in red) for particles streaming along the regular toroidal magnetic field orientation (designated as counter-clockwise when looking at the machine from above). Consequently, the negative velocities (in blue) indicate flows against the regular toroidal magnetic field direction.

In this paper, the C^{2+} radiation intensities and parallel flow velocities will be investigated in different plasma scenarios, i.e. with varying line-averaged electron density $\overline{n}_e$ and input power P_{in}, in attached and detached conditions. The interpretation of the results relies on EMC3-Eirene simulations, but the general tendencies are explained with a simple 1D fluid model.

2. CIS observations

The CIS results reported here are from the most recent W7-X operational campaign (OP1.2b, year 2018). The focus is on plasma experiments performed in the standard magnetic configuration, as for the example in figure 1. The size of the 5 magnetic islands present in the SOL can be controlled with the use of the so-called *control coils*, mounted behind the divertor targets. In particular, when used with a positive current ($I_{cc} > 0$ kA), the control coils enlarge the islands [16]. As these
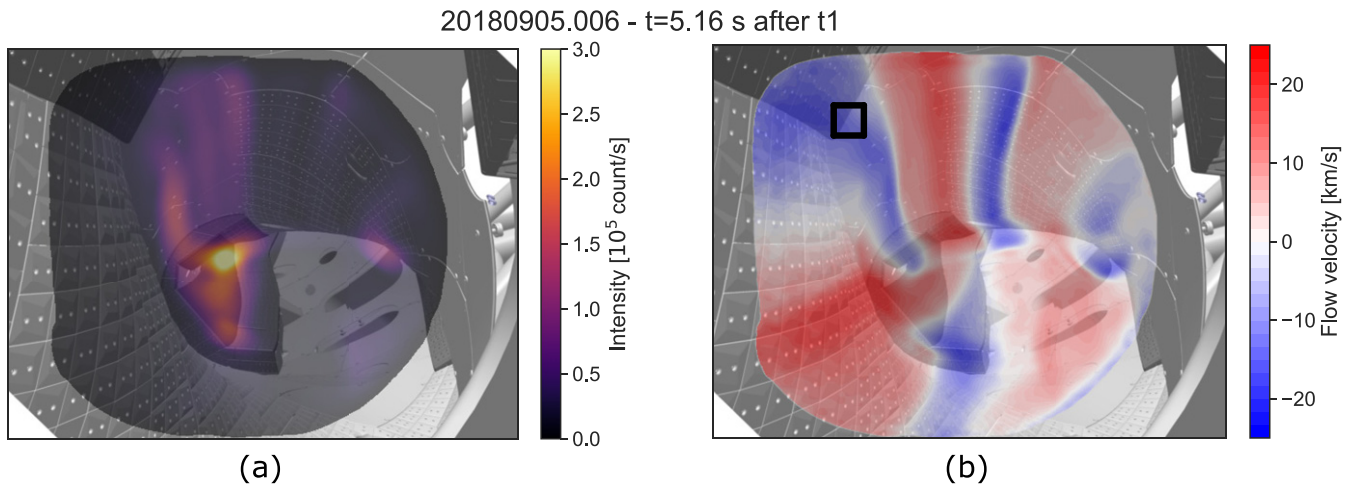
20180905.006 - t=5.16 s after t1

Figure 1. CIS results for the experiment #20180905.006, performed in the standard magnetic configuration ($I_{cc} = 0$ kA). The measurements are overlaid on a CAD model of W7-X. The displayed time point is characterized by input power $P_{ECRH} = 2.5$ MW and line-averaged density $\overline{n}_e = 5.65 \times 10^{19}$ m^{-2}. (*a*) C^{2+} emission intensity, as measured by the C III 465 nm transition line, (*b*) C^{2+} Doppler flow velocity. Positive velocities (in red) represent particle flows along the regular toroidal magnetic field direction, while negative ones (in blue) indicate flows opposite to it. The black square indicates the domain for the signal evaluation in the following figures.

changes in size affect the SOL dynamics [6, 17], the current setting will always be stated. The selected experiments feature only electron cyclotron resonant heating (ECRH) and were performed after boronization, a technique used to substantially decrease the amount of intrinsic impurities (especially oxygen) in the plasma [18]. The data set includes plasmas characterized by different fuelling and density control techniques, such as pre-fill of hydrogen, continuous puffing from the main or the divertor gas fuelling systems, and low-frequency pellet injections.

The C^{2+} radiation intensities and flow velocities are presented in relation with other physics parameters, namely the total plasma radiated power (P_{rad}), the line-averaged density ($\overline{n}_e$), and the peak heat load on the the divertor targets (q_{peak}). The quantities were measured respectively by a bolometer camera (horizontal) [19], by an interferometer [20], and by infra-red cameras [21]. The bolometer camera measures the total plasma radiation from mainly the impurity line emission in the vacuum-ultraviolet and soft x-ray regions (with wavelengths between 300 nm and 0.2 nm). It is installed at a fixed toroidal angle, with lines of sight crossing both the SOL and the plasma core (i.e. covering the entire plasma cross section). The value of P_{rad} is an extrapolation from the measured area to the entire plasma volume under stellarator symmetry conditions, which is supported by EMC3-Eirene simulations [22]. The interferometer features a single line of sight (1.33 m long), which passes through both the SOL and the plasma core as well. Consequently, the values of $\overline{n}_e$ are not equal to the SOL electron density. Nonetheless, given the flat density profiles typical of ECRH heated plasmas [23], the variations in line-averaged density can be used as a proxy for the electron density variations at the *upstream position*, i.e. the SOL region at the closest location to the core plasma. In W7-X attached plasmas, the upstream density is also proportional to the density close to the divertor targets (*downstream position*) in a nearly linear way [5, 24]. Therefore, variations in the interferometer

results are considered representative for density variations at the CIS measurement location. During detachment, the relation between upstream/downstream densities is less straightforward, thus the line-averaged density does not necessarily reflect the plasma conditions where the C^{2+} impurity radiates. Despite these difficulties in interpretation, the CIS observations are here presented with respect to the line-averaged density in both attachment and detachment, due to the lack of an extensive database of SOL density measurements for OP1.2b.

At W7-X, it has been possible to identify the transition to the detached plasma state with an increase of the radiated power fraction $f_{rad} = P_{rad}/P_{ECRH}$. During OP1.2b, in fact, the impurity radiation has been the main drive for the reduction of the thermal power deposited on the targets and for the drop in the divertor particle fluxes, both characteristic of detachment [25]. In particular, it has been observed that the particle fluxes to the divertor begin to decrease with $f_{rad} \approx 0.45$–0.5, and continue diminishing for higher f_{rad} [17, 25, 26]. Therefore, in the following discussion, plasmas featuring $f_{rad} < 0.45$ will be considered attached, while the ones characterized by $f_{rad} \geqslant 0.45$ will be treated as detached or as in transition to detachment. The following analysis considers all the routes to detachment explored in the OP1.2b campaign, namely density scans with main and divertor gas fuelling systems [17, 25, 26], density feedback control with low-frequency pellet injections [25], and impurity seeding [27]. For a more detailed description of the achieved detached state and its characteristics (such as magnitude of the drop of the fluxes, or neutral compression in the divertor area) please refer to [17, 25, 26].

2.1. Attached scenarios: density and power dependence

The C^{2+} radiation intensity measured by CIS shows a strong correlation to the total radiated power P_{rad} and depends on the line-averaged electron density $\overline{n}_e$, as shown in figure 2 (left) for the entire data set, selected as mentioned above. Each data
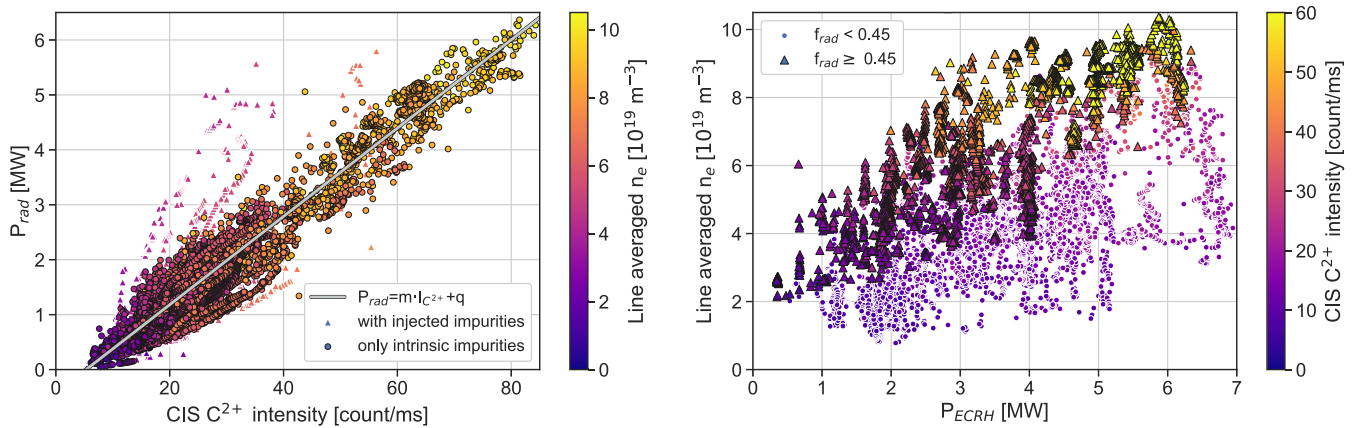
Figure 2. Overview of C^{2+} radiation intensity behaviour throughout the entire operational campaign OP1.2b in the standard magnetic configuration (after boronization). All the variations of field intensity and of control coil current are included. The represented data points are from experiments characterized by $P_{in} = P_{ECRH}$ (no NBI operation) and averaged over a time period of 200 ms. The radiation intensity has been averaged over the full camera chip. (Left) Relation between C^{2+} radiation intensity and radiated power with increasing density. The linear least-squares regression is calculated considering only the experiments without injected impurities ($m = 0.08$, $q = -0.43$, correlation coefficient $r = 0.98$). (Right) C^{2+} radiation intensity variations with density and input power.
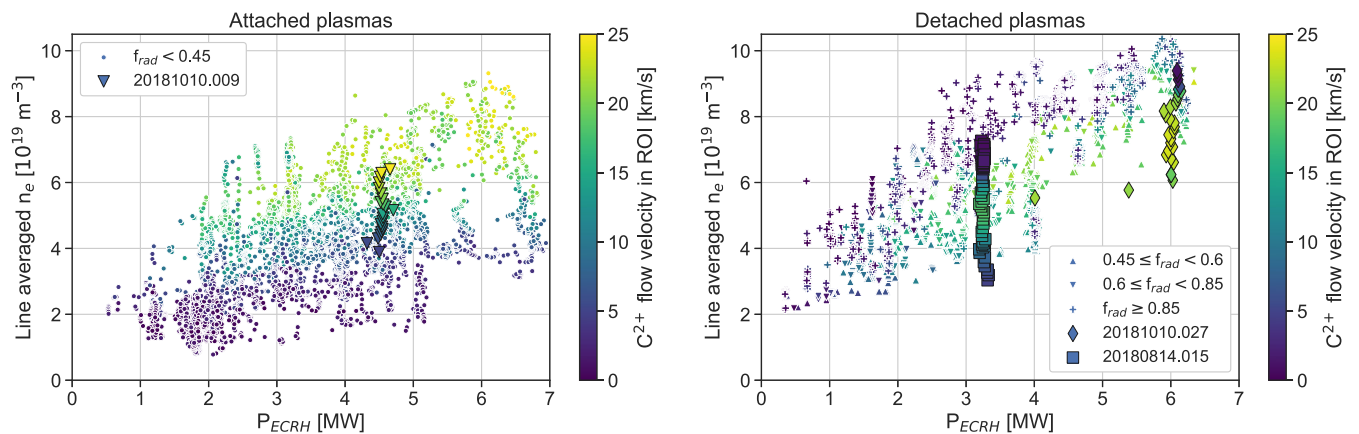
Figure 3. Overview of C^{2+} flow velocity behaviour with respect to input power and electron density throughout the entire operational campaign OP1.2b in the standard magnetic configuration (after boronization). All the variations of field intensity and of control coil current are included. The represented data points are from experiments characterized by $P_{in} = P_{ECRH}$ (no NBI operation) and averaged over a time period of 200 ms. The velocity has been averaged in the domain shown by the black square in figure 1. (Left) Attached plasmas, (right) detached plasmas. The highlighted plasma experiments are shown explicitly in following figures.

point represents the radiation intensity averaged for the full CIS image and over a time period of 200 ms. It can be observed that the C^{2+} radiation intensity shows linear proportionality to P_{rad} in most of the considered cases, reflecting the expectation of carbon as the main radiator in W7-X after boronization [18], and suggesting the importance of the SOL in the total plasma radiation measurement. The data points that diverge from the linear dependence are from the experiments with impurity seeding, which are characterized by puffs of N or Ne with the intent of increasing P_{rad} [27]. Excluding these points, it is possible to perform a linear least-squares regression, so that P_{rad} relates to the C^{2+} radiation intensity ($I_{C^{2+}}$) as:

$$P_{rad} = m \cdot I_{C^{2+}} + q \tag{1}$$

with $m = 0.08$, $q = -0.43$, and correlation coefficient $r = 0.98$. The density dependence of the C^{2+} radiation intensity visible in the colorscale of figure 2 (left) is also

observable in figure 2 (right). Additionally, the latter plot points to an insensitivity of the parameter measured by CIS on P_{ECRH}. These trends could be explained thanks to the strong relation between the C^{2+} radiation intensity and the radiated power: P_{rad} is by definition directly proportional to the density but not to the input power [28].

Similarly, the CIS flow velocity measurements show a clear dependence on electron density and insensitivity on input power. Figure 3 (left) displays the behaviour of the C^{2+} flow velocities with electron density and power again throughout the entire data set, selected as mentioned above. Each data point represents the flow velocities averaged in the domain indicated in figure 1 and over a time period of 200 ms. As previously mentioned, the data have been chosen based on the radiated power fraction $f_{rad} < 0.45$, for which the plasmas can be still considered attached. It can be seen that, at fixed input power and increasing density, the CIS velocities increase,

while at fixed density and increasing power, little or no variation of the velocity magnitude is recorded. The influence of P_{in} on the CIS flow velocities is then only indirect: higher input power allows higher density [29] and, therefore, higher velocities. The behaviour shown here for a selected group of lines of sight has been checked and confirmed in different regions of the measured flow pattern.

2.2. Detached scenarios: intensity rise and velocity drop

During the transition to detachment, the C^{2+} radiation intensity shows a significant rise, maintaining the linear correlation with P_{rad} identified in attached plasmas. On the other hand, the tendency of increasing C^{2+} velocity with increasing $\overline{n}_e$ is reversed, i.e. during detachment the velocity decreases with rising line-averaged density. The overview for intensity and velocity behaviours over the experiments of the entire data set, selected as mentioned above, is shown respectively in figure 2 (right) and figure 3 (right). The general tendencies are also displayed in the case of two selected plasma experiments in figure 4, featuring density scans due to continuous puffing at different P_{ECRH}. It can be seen how the roll-over of the flow velocities and the sharper rise of the radiation intensity, characteristics of detachment, happen in both cases around $f_{rad} = 0.45$. It should be noted that the related necessary densities differ depending on the input power, observation in line with what discussed for figure 3 (left). Figure 5(a) shows more details for one of the chosen experiments: the time evolution of the CIS signals are presented together with the input power P_{ECRH}, the radiated power P_{rad}, the line-averaged density $\overline{n}_e$, and the peak heat load q_{peak}. With reference to q_{peak}, the plasma experiment can be divided into three domains: attached (before 5 s, figures 5(b) and (d)), transition to detachment (5–7.5 s, highlighted), and detached (7.5–13 s, figures 5(c) and (e)). The decrease in flow velocity starts during the transition to detachment, which can be identified by a change in the slope of the peak heat load signal. The sensitivity of the velocity measured by CIS to density changes is also clear in the time interval 8.5–10.5 s, which shows only small variations in the peak heat load trace. The 2D CIS measurements shown in figures 5(b)–(e) confirm that the tendencies are shared by the entire island chain.

The sharp decrease in C^{2+} flow velocities and the rise in C^{2+} radiation intensities are reliably correlated to the detachment transition and can therefore be used as detachment signatures. A velocity drop by at least a factor of 2 has been recorded for all the explored routes to detachment. The magnitude of the decrease is proportional to P_{rad} and the minimum velocity values reached during detachment are observed for $f_{rad} \geqslant 0.85$, as visible in figure 3 (right). The observations in [17, 25, 26], which identify a strong correlation between f_{rad} and the heat and particle fluxes to the target, allow to define degree of detachment as how high f_{rad} is. With this interpretation, it is possible to see how, with increasing input power, a higher line-averaged density is necessary to reach the same degree of detachment, and therefore a similar velocity drop. This explains the dependence of the flow velocities on P_{ECRH} identifiable in figure 3 (right), which is then only indirect.
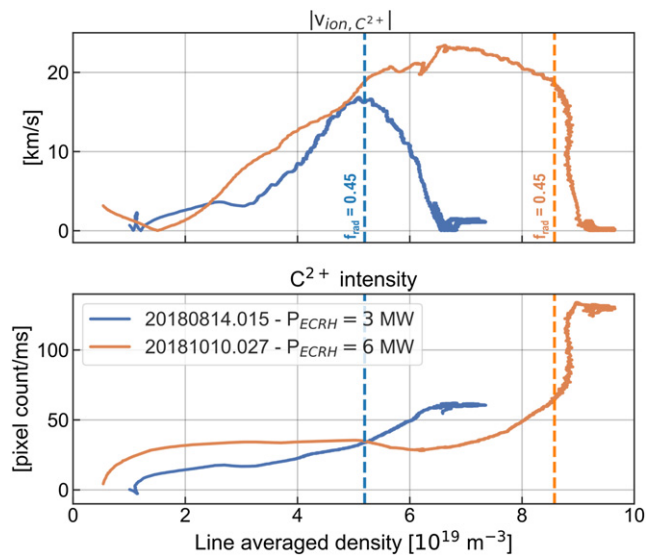
Figure 4. Examples of density dependence for C^{2+} flow velocity and radiation intensity during two density-ramp experiments ending in detachment, both performed in the standard magnetic configuration ($I_{cc} = 2$ kA), but characterized by different input power. The density increase is due to continuous puffing from either the main (#20180814.015) or the divertor (#20181010.027) gas inlet systems. The C^{2+} flow velocity are averaged in the black square domain in figure 1, while the radiation intensity is averaged on the entire CIS image. The dashed lines represent the density at which $f_{rad} = 0.45$.

It should be noted that first direct measurements of SOL plasma densities near the downstream position, based on probes and dispersive spectroscopy [24, 25], suggest that the line-averaged density might not be representative for the plasma conditions in the CIS probing location during detachment. The measured SOL densities, in fact, present a similar roll-over with the transition to the detachment as the one of the C^{2+} flow velocities shown in figure 4 (top), i.e. both quantities increase with increasing line-averaged density during attached plasmas, while showing the opposite tendency in the transition to and during detachment. As these SOL density results are only available for few plasma experiments, the following discussion is still based on the line-averaged density measurements.

3. Dependency of the C^{2+} radiation intensity on the electron density

An analysis of the dependency on the line-averaged electron density of the C^{2+} radiation intensity is carried out due to its strong influence on the CIS measurements and on their interpretation, as well as on the transition to detachment. The $\overline{n}_e$ dependency, observable in figure 2, is to be expected due to the previously mentioned strong relation between the C^{2+} emission and P_{rad}. If only the plasma experiments without seeded impurities are considered, an explicit density dependence can be formulated for the CIS intensity measurements.

The radiated power is defined as

$$P_{rad} = \int n_e n_{imp} \sum_k f_k L_k \, dV \qquad (2)$$

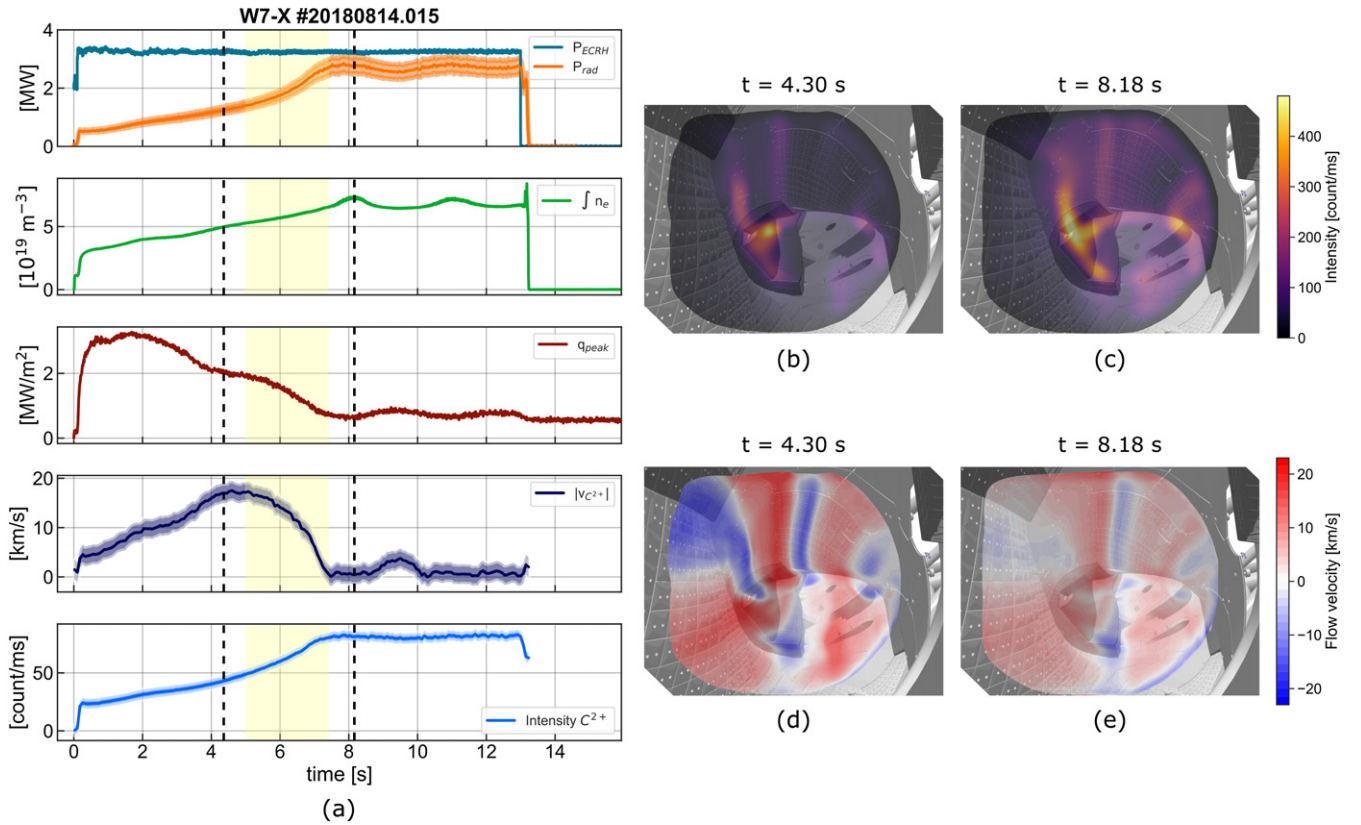**Figure 5.** Data for experiment #20180814.015 performed in the standard magnetic configuration ($I_{cc} = 2$ kA). (*a*) Overview plot for one of the experiments plotted in figure 4, with the transition to detachment highlighted in yellow. The density increase is caused by continuous puffing from the main gas fuelling system. From top to bottom: input power and radiated power, line-averaged density, peak heat load on the divertor targets, C^{2+} flow velocity and radiation intensity. The C^{2+} flow velocity are averaged in the black square domain in figure 1, while the radiation intensity is averaged on the entire CIS image. Examples of CIS frames for attached (*b*, *d*) and detached (*c*, *e*) conditions are also shown.

with n_{imp} as impurity density, f_k as fraction of each impurity ionization state k ($f_k = n_k/n_{imp}$), and L_k as its total radiative cooling rate [28]. All the quantities are integrated on the total plasma volume V. Despite the presence of n_e, equation (2) cannot be directly used to represent the CIS data: n_{imp} is, in fact, a non-trivial function of electron density, being closely related to impurity production and transport properties in the SOL. Moreover, f_k and L_k are not accurately known for each data point. Alternatively, the empirical approach of the P_{rad} multi-tokamak scaling presented in [30] can be adopted, for which P_{rad} is given by:

$$P_{rad} = \frac{1}{\alpha Z^{\delta}}(Z_{eff} - 1)S^{\beta}\overline{n}_e^{\gamma}, \qquad (3)$$

where Z is the main impurity charge, Z_{eff} is the effective plasma ion charge, $\overline{n}_e$ is the line-averaged electron density in 10^{20} m^{-3}, and S is the surface of the radiating plasma volume, assumed to be a uniform shell surrounding the plasma core and estimated by the formula $4\pi^2 rR$ [1]. Equations (2) and (3) are linked by the fact that the information about the plasma impurities is represented by Z and Z_{eff}, while the unknown quantities can be captured by letting free the parameters α, β, γ, δ in the fit. Being formulated for a multi-machine fit, α, β, δ are well determined only when Z and S can vary. This is

not the case when only W7-X experiments with carbon as the main radiator are taken into account: if all the fit parameters are left free, in fact, the estimation of α, β, δ has an unrealistically high error. For this reason, the data has been fit with the simplified model:

$$P_{rad} = \frac{1}{7}(Z_{eff} - 1)S\overline{n}_e^{\gamma} \qquad (4)$$

in which γ is the only free parameter, while the other factors have been set equal to what obtained in [30]. By combining equation (4) and the linear fit represented by equation (1) and shown in figure 2 (left), it is possible to link the C^{2+} radiation intensities measured by CIS to the line-averaged density $\overline{n}_e$. For W7-X, S can be calculated with $r = 0.5$ m and $R = 5.5$ m, while Z_{eff} can be derived from experimental data. During OP1.2b, line-averaged measurements of Z_{eff} were performed [31] and the results can be seen in figure 6 for the same set of experiments represented with dots in figure 2 (left). As Z_{eff} is not available for each CIS data point, the shown fit has been used to include the quantity in equation (4). The tendency of higher Z_{eff} at lower density, visible in figure 6, has been predicted in [6] and thoroughly investigated in [32, 33].

The application of equation (4) to CIS data can be seen in figure 7, where the C^{2+} radiation intensities are plotted against the line-averaged electron density. The data set is
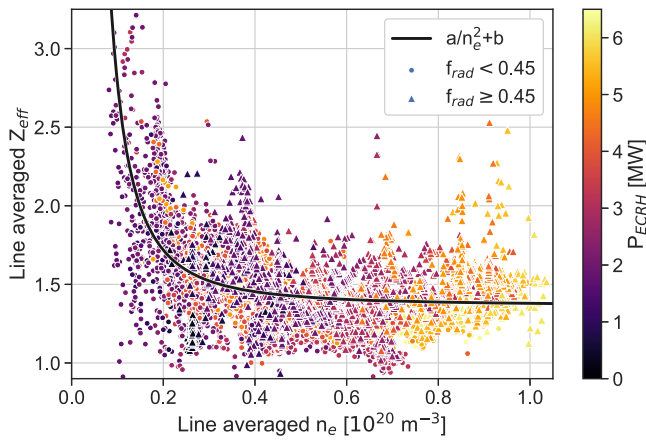
Figure 6. Overview of line-averaged Z_{eff} in relation with the electron density and the input power throughout the entire operational campaign OP1.2b in the standard magnetic configuration (after boronization). All the variations of field intensity and of control coil current are included. The represented data points are from experiments characterized by $P_{in} = P_{ECRH}$ (no NBI operation) and averaged over a time period of 200 ms. The experiments with seeded impurity have been excluded. The fit converged to the values $a = 0.0133 \pm 0.0002$, $b = 1.3672 \pm 0.0032$.

Figure 7. Overview of line-averaged C^{2+} radiation intensity in relation with the electron density and the input power throughout the entire operational campaign OP1.2b in the standard magnetic configuration (after boronization). All the variations of field intensity and of control coil current are included. The represented data points are from experiments characterized by $P_{in} = P_{ECRH}$ (no NBI operation) and averaged over a time period of 200 ms. The experiments with seeded impurity have been excluded. The lines are fit curves based on equation (4). The dashed black line represent the fit with $\gamma = 2$, as in [30], while γ has been left free for the solid green line, converging to the value $\gamma = 2.487 \pm 0.008$.

selected as for figure 2 with the additional condition of considering only the plasma experiments without extrinsic impurities. The two displayed curves suggest that the C^{2+} radiation intensities measured by CIS scale with more than the line-averaged density squared. The figure in fact shows the original multi-machine law, featuring $\gamma = 2$, and the curve based on equation (4), which has $\gamma \approx 5/2$ and appears to better represent the data points. As the result relies on many approximations and assumptions, the absolute value of the fitted exponent should be treated with care. It should be noted that the full investigation has been performed with no distinction between attached and detached scenarios, meaning that equations (1) and (4) are representative for both conditions. Despite no discussion on the underlying physics mechanisms, the trend of C^{2+} radiation intensities with $\overline{n}_e^\gamma$, with $\gamma \geqslant 2$, appears robust and can be used as a reference for the transition to detachment, i.e. as one of its possible actuators in future experiments. Additional radiation scaling studies for W7-X based directly on bolometer data can be found in [34].

4. Physics interpretation for the C^{2+} flow velocity behaviour

In order to physically interpret the CIS flow velocity results shown in the previous sections, it is necessary to understand how representative the C^{2+} impurity behaviour is for the H^+ particle dynamics. This can be achieved relying on EMC3-Eirene modelling. In case of strong coupling between the flows of the two particle species, a 1D fluid model can be formulated for interpreting the CIS measurements.

4.1. Coupling of C^{2+} and H^+ flow velocities

As previously mentioned, the CIS diagnostic probes the impurity velocity in areas of the SOL where the impurity radiation
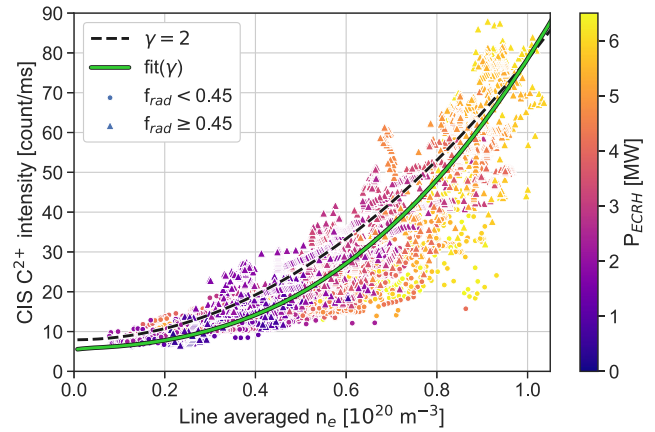
is located. The C^{2+} emission peaks in regions characterized by electron temperatures of 10–20 eV. This range coincides with the one favourable for hydrogen ionisation. The locations of both the C^{2+} emission and the H ionisation can be predicted by EMC3-Eirene and are displayed in figure 8 for the W7-X standard magnetic configuration ($I_{cc} = 0$ kA) at a fixed poloidal cross-section of the machine. The simulations are for different f_{rad}, one mimicking the attached state ($f_{rad} = 0.43$) and the other the detached one ($f_{rad} = 0.80$), but are otherwise characterized by the same parameters, such as input power $P_{in} = 5$ MW, diffusivity $D_\perp = 0.5$ m^2 s^{-1}, and electron and ion thermal conductivities $\chi_e = \chi_i = 1.5$ m^2 s^{-1}. More details on the simulation set-up can be found in [26] (simulation S1). Despite the proximity to the f_{rad} limit used for the experimental data mentioned above ($f_{rad} \approx 0.45$), $f_{rad} = 0.43$ has been chosen for the representation of the attached condition because it is the value at which EMC3-Eirene predicts the maximum recycling flux [17, 26]. Moreover, at this radiated power fraction, it is possible to clearly identify the region of the C^{2+} radiation, otherwise too close to the targets. Focussing the attention on the radial direction from the last closed flux surface (LCFS) to the divertor, it can be seen that, for both attached and detached conditions, the C^{2+} radiation location partially overlaps with the H ionisation region while remaining closer to the targets. The movement of the radiation peak and the extension of the emitting area towards the LCFS at higher f_{rad}, observed also experimentally [17], is in fact accompanied by a shift and an expansion of the H ionisation zone. A friction-dominated scenario is therefore expected for the C^{2+} impurities [35] in both attached and detached plasmas, thanks to their vicinity to a source of H^+, maintained at all the different f_{rad}, and to the low temperature gradients typical of the region where the C^{2+} radiation takes place. This scenario is confirmed by the
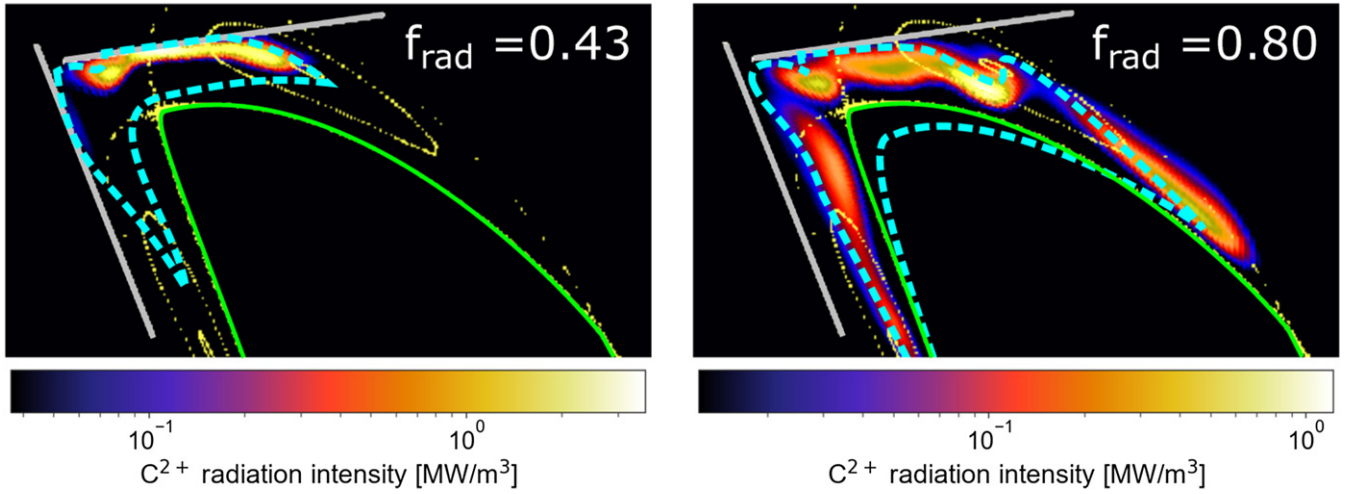
Figure 8. EMC3-Eirene simulations for the C^{2+} radiation intensity distribution (colourmap) with respect to the location of hydrogen ionisation (inside the cyan dashed lines) at a fixed toroidal angle ($\phi = 0°$) and different f_{rad}. The grey lines indicate the divertor targets, while the data in yellow is the Poincaré plot of the magnetic islands in the standard magnetic configuration ($I_{cc} = 0$ kA). The solid green line indicates the LCFS. The adopted input parameters for the simulation are: $P_{in} = 5$ MW, $D_\perp = 0.5$ m^2 s^{-1}, $\chi_e = \chi_i = 1.5$ m^2 s^{-1}. More details on the simulation set-up can be found in [26] (simulation S1).

CIS experimental data, in which the C^{2+} impurities are measured to stream towards the closest divertor target with no flow reversal being observed for the entire range of explored f_{rad}, suggesting a strong coupling of the H^+ and C^{2+} flows.

If the ion thermal force remains negligible at different f_{rad}, the C^{2+} impurities are a good proxy to examine the hydrogen ion parallel flow behaviour in the SOL. Impurity transport simulation in EMC3-Eirene calculates the parallel force balance for the carbon impurities. The force magnitude can be provided as output. The result for the C^{2+} impurity is here expressed in terms of velocities, representing the major contributors to the balance. v_{C2+} is in fact approximately equal to $v_{H+} - v_{ion,thermal}$, where v_{H+} represents the friction between H^+ and C^{2+}, and $v_{ion,thermal}$ depends on the SOL ion temperature gradient and acts against the coupling of the H^+ and C^{2+} flows [1, 35]. The terms are shown in figure 9 for the same f_{rad} cases, magnetic configuration, simulation input parameters, and machine cross section as in figure 8. It can be seen that both velocities drop with increasing f_{rad}, and that the contribution of $v_{ion,thermal}$ remains negligible in the majority of the island chain. The restricted location and the modest magnitude of the ion thermal force is a consequence of the strong perpendicular transport typical of the W7-X SOL, which tend to flatten the parallel ion temperature gradient [6]. Given the insignificant deviation of v_{C2+} from v_{H+} predicted by EMC3-Eirene for the W7-X SOL, it appears legitimate to use the observations of the C^{2+} impurities to gain information about the hydrogen ion parallel flow behaviour.

It should be noted that the EMC3-Eirene simulations for the C^{2+} radiation intensity do not take into account charge exchange processes between carbon ions and hydrogen atoms. This implies that the distributions in figure 8 can differ from the experiments, which will be characterized by broader regions occupied by the radiation, especially at higher f_{rad}. Nonethe-

less, the link between the C^{2+} emission and the H ionisation locations is maintained, since the carbon radiation will cool the plasma, allowing ionisation in a wider area.

The above-mentioned variations in the locations of the C^{2+} radiation and H ionisation are a consequence of the evolution of the SOL plasma parameters, such as the electron temperature (T_e), during the transition to detachment. These changes reflect on the parallel ion velocity as well, as shown in figure 10, displaying $v_{H+\parallel}$ and T_e profiles along an open field line extracted from the same simulations used for figures 8 and 9. The highlighted areas indicate the expected locations of maximum C^{2+} emission, and therefore where the CIS measurements take place. For $f_{rad} = 0.8$, the temperature gradient becomes shallow between the carbon radiation front and the targets (between -200 and -80 m and between 80 and 200 m), a phenomenon that contributes to the flattening of the velocity profile in the same region. These changes imply that, despite the movement of the probing location, the CIS measurements can still be representative for the main ion velocities in the regions close to the divertor targets.

The robust coupling between the C^{2+} impurity and the H^+ ions suggests that the tendencies highlighted by the CIS measurements can be related to the behaviour of the main ion flows. Therefore, a simple 1D fluid model can be used to gain some first insight into the leading physics processes. However, it should be noted that the following simple model will only provide an intuitive explanation of the major trends observed in the C^{2+} flow velocity, i.e. it will not be able to capture the entire physics picture in full details. Despite the fact that both the CIS measurements and the EMC3-Eirene modelling show similar behaviours, a more precise interpretation of the parallel flow velocity drop with higher f_{rad} at the C^{2+} radiation location is still being developed and it is currently left for the future.
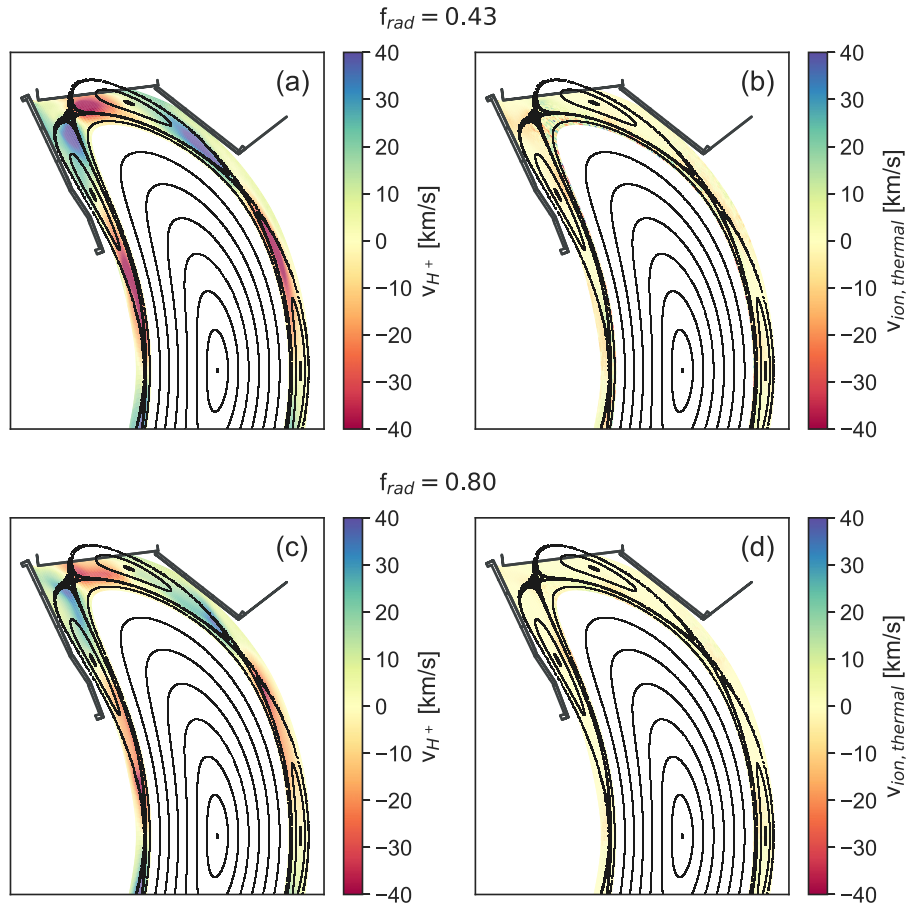
$f_{rad} = 0.43$

$f_{rad} = 0.80$

Figure 9. EMC3-Eirene simulations for friction (v_{H+}) and thermal ($v_{ion,thermal}$) contributions to the C^{2+} impurity flow velocity at a fixed toroidal angle ($\phi = 0°$) and different f_{rad}. The simulation results are shown only for the SOL domain. The grey lines indicate the divertor targets and the baffles, while the data in black is the Poincaré plot of the magnetic field in the standard magnetic configuration ($I_{cc} = 0$ kA). The simulation parameters are the same as for figure 8. (*a*) Friction term at $f_{rad} = 0.43$; (*b*) thermal force term at $f_{rad} = 0.43$; (*c*) friction term at $f_{rad} = 0.80$; (*d*) thermal force term at $f_{rad} = 0.80$.

4.2. 1D fluid model description

In order to investigate whether a 1D model can predict trends in the ion parallel velocity behaviour similar to the ones measured by CIS, the SOL H^+ ion flux $\Gamma = nv_\parallel$ will be examined. Γ should satisfy the continuity equation, which in steady-state conditions is

$$\frac{d\Gamma}{dx} \equiv \frac{d(nv_\parallel)}{dx} = S_p \qquad (5)$$

with x as the direction along the SOL open magnetic field line, and S_p as the particle source term. In the regions probed by CIS, the major contributor to S_p is the ionisation of neutral H atoms (S_i), which happens predominantly in the W7-X SOL for $f_{rad} < 0.9$, as shown in [26] and as suggested by figure 8. The cross-field transport, normally included in the description of the SOL dynamics as both source and sink for the parallel transport [1], is here considered constant during the changes in plasma conditions discussed in section 2 (density variations and transition to detachment). Therefore, any cross-field term is neglected in the current discussion and the identification of trends for the ion parallel velocity is reduced to the study of the ionisation source. Even if changes in the SOL pressure gradient are not directly considered into the following discussion,

their occurrence is expected to influence the ionisation source term.

Equation (5) implies that variations in S_i will be followed by changes in the ion flux, but not necessarily in the parallel velocity. Consequently, additional details are required for the interpretation of the CIS measurements. S_i is defined as [1]:

$$S_i = nn_n\langle\sigma v_e\rangle, \qquad (6)$$

where $n = n_i = n_e$ is the SOL density where the ionisation takes place, n_n is the neutral density, and $\langle\sigma v_e\rangle$ is the ionisation rate coefficient. The neutral density n_n is not an entirely free parameter: empirically, it appears to be influenced by the input power and has an even stronger dependency on n. If a clear relation between n and n_n can be found, the combination of equations (5) and (6) can be used to learn more about the dependence of $v_\parallel$ on density.

In attached conditions, the influence of power on the neutral density is non-negligible due to the W7-X uncooled divertor, for which increasing P_{ECRH} often leads to outgassing of hydrogen atoms due to higher deposited heat on the targets. If plasmas with stable input power are considered, the dependence of n_n on n can be identified experimentally. An example of such a case is the density ramp experiment shown
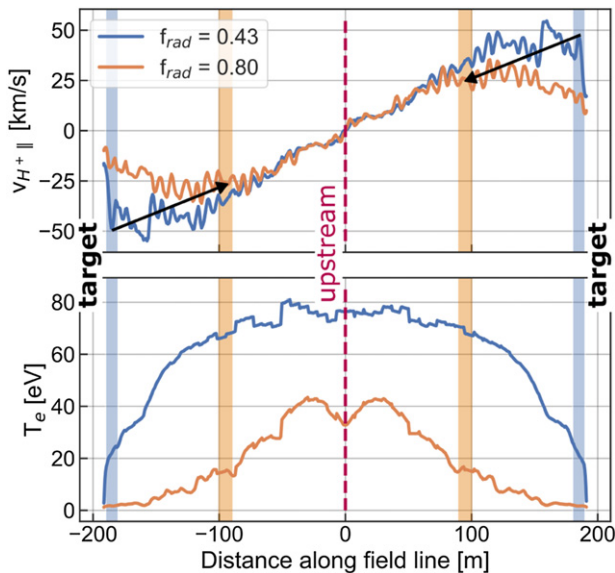
Figure 10. EMC3-Eirene simulation for H^+ flow velocities and T_e along the one open magnetic field line. The simulation parameters are the same of figure 8. The dashed red line represents the closest location to the LCFS along the magnetic field line. The two divertor targets connected by the open field line are placed at -200 and 200 m. The highlighted regions mimic the location of the C^{2+} radiation for the two f_{rad} cases. The two black arrows indicate the change in the CIS probing regions. The discontinuities in the signals are caused by the profile mapping method used in post-processing. This behaviour does not occur during the original EMC3-Eirene particle tracing, for which a more robust mapping technique is used.
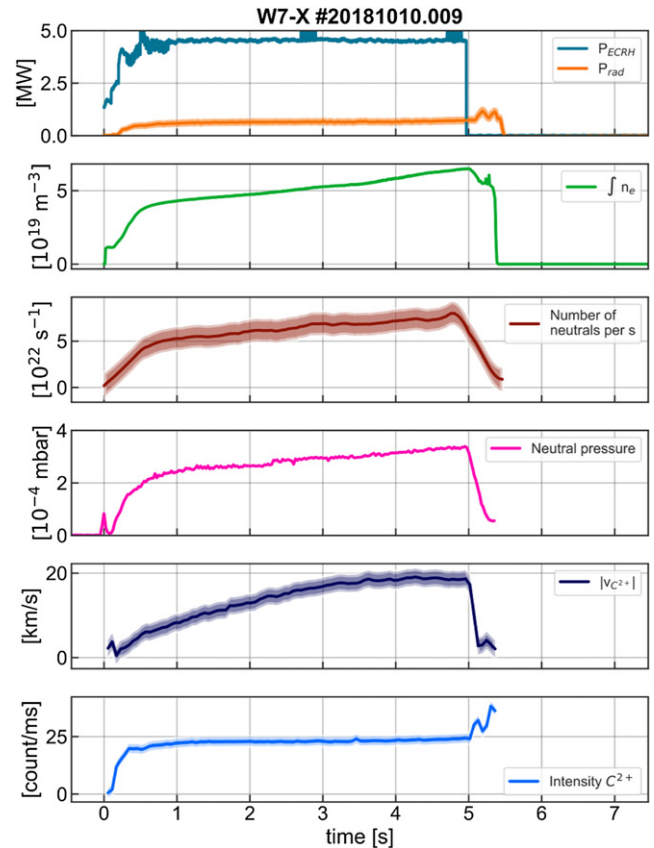

Figure 11. Overview plot for the experiment #20181010.009 performed in the standard magnetic configuration ($I_{cc} = 0$ kA). The density rise is caused by continuous puffing from the main gas inlet system. From top to bottom: input power and radiated power, line-averaged density, total number of neutral particles per second (the S/XB coefficients used in the calculation have been considered constant over the whole experiment), neutral pressure in the divertor area, C^{2+} flow velocity and radiation intensity. The C^{2+} flow velocity are averaged in the black square domain in figure 1, while the radiation intensity is averaged on the entire CIS image.

in figure 11, in which $\overline{n}_e$ is increased with continuous puffing from the main gas fuelling system. The rise of the C^{2+} flow velocities with increasing density is shown by the CIS data. The measurements representing the neutral density variations are obtained with H_α cameras [36, 37] and with pressure gauges [38], which monitor respectively the number of neutral particles ionizing per second and the neutral pressure in the divertor area. A comparison between the evolution of these quantities and $\overline{n}_e$ (proportional to the downstream density in attached conditions) suggests that the neutral density scales nearly linearly with the SOL density. In view of this example, it is possible to consider $n_n \sim Cn$ with C as a proportionality constant, so that equation (5) becomes:

$$\frac{\mathrm{d}(nv_\parallel)}{\mathrm{d}x} \sim Cn^2 \langle \sigma v_e \rangle. \tag{7}$$

Therefore, in attached scenarios, an increase of the SOL density ($\propto \overline{n}_e$) leads to an increase of $v_\parallel$ (also visible in figure 11) in order to satisfy the continuity equation, as the ionisation source scaling with n is stronger than for the particle flux Γ ($S_i \sim n^2$, $\Gamma \sim n$). It should be noted that equation (7) does not depend explicitly on the input power, similarly to what was observed in the CIS measurements of attached plasmas (see figure 3 (left) and its discussion).

For detachment, the link between the particle flux and the ionisation source is expected to remain valid, but the simplification leading to equation (7) might not hold, since it is unclear whether the linear relation between n and n_n is maintained.

Nonetheless, if S_i were to drop for detached plasmas, either n or $v_\parallel$ or both parameters would need to decrease. A prediction for S_i can be formulated based on the SOL global power balance: S_i is, in fact, regulated by the fraction of input power available for ionisation. The SOL global power balance can be expressed as [26, 39]:

$$P_{in} = P_t + P_{\varepsilon_i} + P_{rad}, \tag{8}$$

where P_{in} is the power entering the SOL, P_t is the power deposited on the divertor targets, P_{ε_i} is the power loss due to plasma interactions with neutral particles (including ionisation), and P_{rad} is the radiated power. Equation (8) is particularly helpful in the interpretation of the detachment measurements, as in this case the power balance can be further simplified: P_t can be neglected and the input power will be divided only between P_{rad} and P_{ε_i}. As P_{rad} is a significant fraction of P_{in} during detachment at W7-X, the power available for ionisation is limited, which already hints at a reduction of the ion flux. In first approximation and in steady state conditions, the ion flux to the target Γ_t can be considered equal to the recycling flux

in the SOL, implying that each ion absorbed by the divertor targets is released as neutral particle. Under this assumption of 100% recycling, it is possible to express explicitly P_{ε_i} and therefore identify the expected behaviour of $nv_\parallel$. The term is in fact defined as

$$P_{\varepsilon_i} = \varepsilon_i \Gamma_t = \varepsilon_i \int_t nv_\parallel \, ds, \qquad (9)$$

where ε_i is the energy cost for the electrons–neutral interactions (including ionisation, dissociation, excitation) and Γ_t is evaluated on the target surfaces. With A_t as total surface of interaction between the incoming ions and the targets, equation (9) simplifies to:

$$P_{\varepsilon_i} \approx \varepsilon_i \langle nv_\parallel \rangle_t A_t. \qquad (10)$$

By considering equations (8) and (10), in detached plasmas $\langle nv_\parallel \rangle_t$ is the result of:

$$\langle nv_\parallel \rangle_t \approx \frac{1}{A_t} \frac{P_{in} - P_{rad}}{\varepsilon_i}. \qquad (11)$$

Detachment simulations by EMC3-Eirene indicate that ε_i is constant at $f_{rad} > 0.6$ in the W7-X standard magnetic configuration [26]. Therefore, for fixed P_{in} and increasing P_{rad}, the ion flux has to decrease. This reduction can be achieved with diminishing $v_\parallel$ and/or SOL densities. Experiments show a decrease of the two parameters simultaneously: both the CIS flow velocity observations and the recent downstream density measurements mentioned above (see section 2.2 and [24, 25]), in fact, present a dependency inversely proportional to $P_{rad} \propto \overline{n}_e^\gamma$ (see section 3) in the transition to and during detachment. The underlying mechanisms for the necessity of a reduction of both n and $v_\parallel$ are still under investigation.

It should be noted that the flow velocity drop with detachment have been previously reported for the DIII-D tokamak as well [40], suggesting that similar physical principles to the ones invoked here for the interpretation of the W7-X measurements may apply also to other fusion devices.

5. Conclusions

The C^{2+} impurity radiation intensity and flow velocity have been monitored throughout the entire last operational campaign of W7-X with the CIS diagnostic. An overview over the full data set has been given with the intention of identifying the major trends of the two parameters. The C^{2+} radiation intensity shows a strong correlation with the radiated power P_{rad}, which could be used to recognize a line-averaged density scaling for the parameter measured by CIS. The tendency $I_{C^{2+}} \propto \overline{n}_e^\gamma$ with $\gamma \geqslant 2$ is consistent in both attached and detached plasma scenarios. On the other hand, the C^{2+} flow velocities behave differently in the two regimes: during attachment, the velocities increase with increasing line-averaged electron densities, while during detachment the trend is reversed. The 2D nature of the CIS measurements allows a confirmation of these tendencies for the full magnetic island chain of W7-X. It should be noted that, in detached conditions, the line-averaged density is not necessarily proportional to the plasma density

at the location probed by CIS. Nonetheless, it has been used due to the lack of an extensive database of SOL density measurements for OP1.2b. Additional direct measurements of SOL densities are necessary to push the experimental investigations further.

The mentioned general behaviour of the C^{2+} impurity, well coupled with the main plasma ions, can be explained in first approximation with a simple 1D fluid model, in which the hydrogen ionisation source term plays a central role. By assuming a constant cross-field transport, it is possible to find a description capturing the major trends observed in the experiments. The CIS results combined with the 1D model, therefore, suggest that the ionisation source is the main contributor to the particle dynamics in the region where the measurements take place. The validity limits of the assumption on the cross-field transport role must still be assessed with future modelling. Additional EMC3-Eirene support will also help in reaching a full quantitative understanding of the convective contribution to the divertor heat loads, represented by the particle parallel velocity. Further measurements are required to confirm the role of the hydrogen ionization source, currently considered central. In particular, detailed studies of the SOL pressure gradient and its variations with density, input power, and radiated power fraction, will help in extending the simple model presented here to a more comprehensive SOL physics analysis.

ORCID iDs

V. Perseo https://orcid.org/0000-0001-8473-9002
V. Winters https://orcid.org/0000-0001-8108-7774
Y. Feng https://orcid.org/0000-0002-3846-4279
S.A. Bozhenkov https://orcid.org/0000-0003-4289-3532
K.J. Brunner https://orcid.org/0000-0002-0974-0457
P. Drewelow https://orcid.org/0000-0003-0121-9058
Y. Gao https://orcid.org/0000-0001-8576-0970
D. Gradic https://orcid.org/0000-0002-6109-9345
U. Hergenhahn https://orcid.org/0000-0003-3396-4511
M.W. Jakubowski https://orcid.org/0000-0002-6557-3497
T. Kremeyer https://orcid.org/0000-0002-6383-944X
D.M. Kriete https://orcid.org/0000-0002-3657-2911
S. Kwak https://orcid.org/0000-0001-7874-7575
H. Niemann https://orcid.org/0000-0003-0300-1060
A. Pavone https://orcid.org/0000-0003-2398-966X
G. Schlisio https://orcid.org/0000-0002-5430-0645
D. Zhang https://orcid.org/0000-0002-5800-4907
T. Sunn Pedersen https://orcid.org/0000-0002-9720-1276

References

[1] Stangeby P.C. 2000 *The Plasma Boundary of Magnetic Fusion Devices* (Bristol: Institute of Physics Publishing)

[2] LaBombard B. *et al* (the Alcator Group) 2004 Transport-driven scrape-off-layer flows and the boundary conditions imposed at the magnetic separatrix in a tokamak plasma *Nucl. Fusion* **44** 1047

[3] Jaervinen A.E., Allen S.L., Leonard A.W., McLean A.G., Moser A.L., Rognlien T.D. and Samuell C.M. 2020 Role of poloidal $E \times B$ drift in divertor heat transport in DIII-D *Contrib. Plasma Phys.* **60** e201900111

[4] Renner H., Sharma D., Kißlinger J., Boscary J., Grote H. and Schneider R. 2004 Physical aspects and design of the Wendelstein 7-X divertor *Fusion Sci. Technol.* **46** 318

[5] Feng Y., Sardei F., Grigull P., McCormick K., Kisslinger J. and Reiter D. 2006 Physics of island divertors as highlighted by the example of W7-AS *Nucl. Fusion* **46** 807–19

[6] Feng Y., Kobayashi M., Lunt T. and Reiter D. 2011 Comparison between stellarator and tokamak divertor transport *Plasma Phys. Control. Fusion* **53** 024009

[7] Porter G.D., Rognlien T.D., Rensink M.E., Loarte A., Asakura N., Takenaga H. and Matthews G. 2003 Simulation of the effect of plasma flows in DIII-D, JET, and JT-60U *J. Nucl. Mater.* **313–316** 1085–8

[8] Chankin A.V. *et al* 2007 A possible role of radial electric field in driving parallel ion flow in scrape-off layer of divertor tokamaks *Nucl. Fusion* **47** 762–72

[9] Howard J. 2010 Coherence imaging spectro-polarimetry for magnetic fusion diagnostics *J. Phys. B: At. Mol. Opt. Phys.* **43** 144010

[10] Perseo V., Gradic D., König R., Ford O.P., Killer C., Grulke O. and Ennis D.A. 2020 Coherence imaging spectroscopy at Wendelstein 7-X for impurity flow measurements *Rev. Sci. Instrum.* **91** 013501

[11] Gradic D. 2018 Doppler coherence imaging of ion dynamics in the plasma experiments VINETA.II and ASDEX upgrade *PhD Thesis* Technische Universität, Berlin

[12] Perseo V. 2020 Impurity flow measurements with coherence imaging spectroscopy at Wendelstein 7-X *PhD Thesis* Universität Greifswald

[13] Perseo V. *et al* 2019 Direct measurements of counter-streaming flows in a low-shear stellarator magnetic island topology *Nucl. Fusion* **59** 124003

[14] Pedersen T.S. *et al* 2018 First results from divertor operation in Wendelstein 7-X *Plasma Phys. Control. Fusion* **61** 014035

[15] Geiger J., Beidler C.D., Feng Y., Maaßberg H., Marushchenko N.B. and Turkin Y. 2014 Physics in the magnetic configuration space of W7-X *Plasma Phys. Control. Fusion* **57** 014004

[16] Bozhenkov S.A., Otte M., Biedermann C., Jakubowski M., Lazerson S.A., Sunn Pedersen T. and Wolf R.C. 2018 Measurements and correction of the 1/1 error field in Wendelstein 7-X *Nucl. Fusion* **59** 026004

[17] Schmitz O. *et al* 2021 Stable heat and particle flux detachment with efficient particle exhaust in the island divertor of Wendelstein 7-X *Nucl. Fusion* **61** 016026

[18] Sereda S. *et al* 2020 Impact of boronizations on impurity sources and performance in Wendelstein 7-X *Nucl. Fusion* **60** 086007

[19] Zhang D. *et al* 2010 Design criteria of the bolometer diagnostic for steady-state operation of the W7-X stellarator *Rev. Sci. Instrum.* **81** 10E134

[20] Brunner K.J. *et al* 2018 Real-time dispersion interferometry for density feedback in fusion devices *J. Inst.* **13** P09002

[21] Sitjes A.P. *et al* 2019 Observation of thermal events on the plasma facing components of Wendelstein 7-X *J. Inst.* **14** C11002

[22] Zhang D. *et al* 2019 First observation of a stable highly dissipative divertor plasma regime on the Wendelstein 7-X stellarator *Phys. Rev. Lett.* **123** 025002

[23] Bozhenkov S.A. *et al* 2020 High-performance plasmas after pellet injections in Wendelstein 7-X *Nucl. Fusion* **60** 066011

[24] Reimold F. *et al* 2021 Poster: experimental indications of high-recycling and the role of pressure and power dissipation in the detachment evolution at Wendelstein 7-X *Preprint: 28th 2020 IAEA Fusion Energy Conf.* 10-15 May 2021) (https://fec2020.fr/) (Virtual

[25] Jakubowski M. *et al* 2021 Overview of the results from divertor experiments with attached and detached plasmas at Wendelstein 7-X and their implications for steady-state operation *Nucl. Fusion* **61** 106003

[26] Feng Y. *et al* 2021 Understanding detachment of the W7-X island divertor *Nucl. Fusion* **61** 086012

[27] Effenberg F. *et al* 2019 First demonstration of radiative power exhaust with impurity seeding in the island divertor at Wendelstein 7-X *Nucl. Fusion* **59** 106020

[28] Mavrin A.A. 2017 Radiative cooling rates for low-Z impurities in non-coronal equilibrium state *J. Fusion Energy* **36** 161–72

[29] Fuchert G. *et al* 2020 Increasing the density in Wendelstein 7-X: benefits and limitations *Nucl. Fusion* **60** 036020

[30] Matthews G.F. *et al* 1997 Scaling radiative plasmas to ITER *J. Nucl. Mater.* **241–243** 450–5

[31] Pavone A. *et al* 2019 Measurements of visible bremsstrahlung and automatic Bayesian inference of the effective plasma charge Z_{eff} at W7-X *J. Inst.* **14** C10003

[32] Winters V. 2019 Carbon sourcing and transport in the island divertor of Wendelstein 7-X *PhD Thesis* University of Wisconsin–Madison

[33] Winters V. *et al* 2021 Evidence of enhanced carbon retention with density in the island divertor of Wendelstein 7-X (in preparation)

[34] Zhang D. *et al* 2021 Plasma radiation behavior approaching high-radiation scenarios in W7-X *Nucl. Fusion* (accepted)

[35] Feng Y. *et al* 2009 Comparative divertor-transport study for helical devices *Nucl. Fusion* **49** 095002

[36] Kremeyer T. 2019 Particle fueling and exhaust in the Wendelstein 7-X island divertor *PhD Thesis* The University of Wisconsin–Madison

[37] Kremeyer T. *et al* 2021 Global particle balance to analyze fueling, exhaust, recycling and particle confinement at Wendelstein 7-X *Nucl. Fusion* (in review)

[38] Wenzel U., Schlisio G., Mulsow M., Pedersen T.S., Singer M., Marquardt M., Pilopp D. and Rüter N. 2019 Performance of new crystal cathode pressure gauges for long-pulse operation in the Wendelstein 7-X stellarator *Rev. Sci. Instrum.* **90** 123507

[39] Pitcher C.S. and Stangeby P.C. 1997 Experimental divertor physics *Plasma Phys. Control. Fusion* **39** 779–930

[40] Howard J. *et al* 2011 Coherence imaging of flows in the DIII-D divertor *Contrib. Plasma Phys.* **51** 194–200